Propagating insulator-to-metal transition in the wake of photoinduced strain waves in a Mott material

Tatsuya Amano, Danylo Babich, Ritwika Mandal, Julio Guzman-Brambila, Alix Volte, Elzbieta Trzop, Marina Servol, Ernest Pastor, Maryam Alashoor, Jorgen Larsson, et al.

▶ To cite this version:

Tatsuya Amano, Danylo Babich, Ritwika Mandal, Julio Guzman-Brambila, Alix Volte, et al.. Propagating insulator-to-metal transition in the wake of photoinduced strain waves in a Mott material. 2023. hal-04308157

HAL Id: hal-04308157
https://hal.science/hal-04308157

Preprint submitted on 27 Nov 2023

Propagating insulator-to-metal transition in the wake of photoinduced strain waves in a Mott material

Maciej Lorenc (maciej.lorenc@univ-rennes1.fr)
CNRS https://orcid.org/0000-0002-6877-8631
Tatsuya AMANO
Department of Physics, Tohoku University
Danylo Babich
Nantes Université, CNRS, Institut des Matériaux de Nantes Jean Rouxel, IMN
Ritwika MANDAL
Univ Rennes, CNRS, IPR (Institut de Physique de Rennes)
Julio Guzman-Brambila
Nantes Université, CNRS, Institut des Matériaux de Nantes Jean Rouxel, IMN
Alix Volte
Univ Rennes, CNRS, IPR (Institut de Physique de Rennes)
Elzbieta Trzop
Univ Rennes, CNRS, IPR (Institut de Physique de Rennes)
Marina Servol
Univ Rennes, CNRS, IPR (Institut de Physique de Rennes)
Ernest Pastor
Institut de Physique de Rennes, CNRS-Centre national de la recherche scientifique
https://orcid.org/0000-0001-5334-6855
Maryam Alashoor
Univ Rennes, CNRS, IPR (Institut de Physique de Rennes)
Jorgen Larsson
Lund University https://orcid.org/0000-0001-9598-8493
Andrius Jurgilaitis
Lund University
Van Pham
Lund University
David Kroon
Lund University
John Carl Ekström
MAX IV Laboratory, Lund University

Byungnam Ahn
MAX IV Laboratory, Lund University
Céline Mariette
ESRF, The European Synchrotron
Matteo Levantino
ESRF - The European Synchrotron https://orcid.org/0000-0002-1224-4809
Mickael Kozhaev
ESRF, The European Synchrotron
Julien Tranchant
Université de Nantes CNRS
Benoît Corraze
Institut des Matériaux Jean Rouxel
Laurent Cario
Institut des Matériaux Jean Rouxel https://orcid.org/0000-0001-5720-4395
Vinh Ta Phuoc
GREMAN—UMR 7347 CNRS, Université de Tours
Rodolphe Sopracase
GREMAN—UMR 7347 CNRS, Université de Tours
Mathieu Grau
GREMAN—UMR 7347 CNRS, Université de Tours
Hirotake Itoh
Tohoku University https://orcid.org/0000-0002-3371-9316
Yohei Kawakami
Tohoku University
Yuto Nakamura
Nagoya University
Hideo Kishida
Nagoya University
Herve Cailleau
University Rennes 1
Shinichiro Iwai
Tohoku University https://orcid.org/0000-0002-5713-1859
Etienne Janod
Institut des Matériaux de Nantes Jean Rouxel (IMN) https://orcid.org/0000-0002-2430-9542

Article

Keywords:

Posted Date: September 12th, 2023

DOI: https://doi.org/10.21203/rs.3.rs-3239079/v1

Additional Declarations: There is **NO** Competing Interest.

Propagating insulator-to-metal transition in the wake of photoinduced strain waves in a Mott material

Tatsuya Amano[1], Danylo Babich[2], Ritwika Mandal[3], Julio Guzman-Brambila[2,3,8], Alix Volte[3,6,8], Elzbieta Trzop[3,9], Marina Servol[3,9], Ernest Pastor[3,9], Maryam Alashoor[3], Jörgen Larsson[6,7], Andrius Jurgilaitis[6], Van-Thai Pham[6], David Kroon[6], John Carl Ekström[6], Byungnam Ahn[6], Céline Mariette[8], Matteo Levantino[8], Mickael Kozhaev[7], Julien Tranchant[2,9], Benoit Corraze[2,9], Laurent Cario[2,9], Vinh Ta Phuoc[4,9], Rodolphe Sopracase[4], Mathieu Grau[4], Hirotake Itoh[1,9], Yohei Kawakami[1,9], Yuto Nakamura[5], Hideo Kishida[5], Hervé Cailleau[3,9,*], Maciej Lorenc[3,9*], Shinichiro Iwai[1,9*], Etienne Janod[2,9*]

[1] Department of Physics, Tohoku University, Sendai 980-8578, Japan
[2] Nantes Université, CNRS, Institut des Matériaux de Nantes Jean Rouxel, IMN, F-44000 Nantes, France
[3] Univ Rennes, CNRS, IPR (Institut de Physique de Rennes) – UMR 6251, 35000 Rennes, France
[4] GREMAN—UMR 7347 CNRS, Université de Tours, Tours, France
[5]Department of Applied Physics, Graduate School of Engineering, Nagoya University, Nagoya, Aichi 464-8603, Japan
[6] MAX IV Laboratory, Lund University, P.O. Box 118, SE-221 00 Lund, Sweden
[7] Department of Physics, Lund University, P.O. Box 118, SE-221 00 Lund, Sweden
[8] ESRF, The European Synchrotron, 71 Avenue des Martyrs, CS40220, 38043 Grenoble Cedex 9, France
[9] CNRS, Univ Rennes, DYNACOM (Dynamical Control of Materials Laboratory) - IRL2015, The University of Tokyo, 7-3-1 Hongo, Tokyo 113-0033, Japan

* corresponding authors

Ultrafast physics opens new avenues for directing materials to different functional macroscopic states on non-thermal dynamical pathways. In any phase transition involving volume and/or ferroelastic deformation, an often overlooked mechanism emerges whereby photoinduced elastic waves drive the transition. However, a comprehensive physical picture of transformation dynamics which includes acoustic scale propagation remained elusive. Here we show that such strain wave mechanism drives the ultrafast insulator-to-metal phase transition (IMT) in the V_2O_3 Mott material. We discuss the underlying physics based on time-resolved optical reflectivity and X-ray diffraction probing granular thin films. We evidence the role of strain wave mechanisms in ultrafast changes either with or without symmetry breaking. We reveal inverse ferroelastic shear occurring before the IMT propagating in the wake of compressive strain wave. These dynamics are shown to be governed by the domain size and the film thickness, respectively. A fluence threshold is evidenced for the onset of IMT at macroscopic scale, as well as phase separation at intermediate fluence and complete transformation at saturating fluence. We clarify the morphological conditions for the ultrafast IMT that is favoured in granular thin films, and hindered in single crystals. The resulting physical

picture sheds new light on the ultrafast phase transitions in quantum materials and future devices based on Mott insulators.

The capability to direct a material to another phase along a coherent transformation pathway raises questions on the dynamical limits of photoinduced phase transitions. When atomic displacements in a unit cell play a dominant role, the ultimate time scale is governed by the period of coherent zone-center optical phonons [1-3]. For phase transitions involving volume change and/or shear deformations of the lattice, this limit is imposed by the propagation of strain waves. This underlines the role in coherent dynamics of long-wavelength acoustic phonons, the counterpart of optical phonons. However, in contrast with many coherent dynamics along established transition pathways [4,5], the abilility of strain waves to transform the macroscopic state of a material has been little explored. Some recent results highlighted the role of volume expansion dynamics in photoinduced processes for different materials exhibiting first order isostructural (isosymmetric) phase transitions involving an electronic change [6-8], but providing a comprehensive view remains a challenge. Many quantum materials exhibit phase transitions coupling an isosymmetric Mott IMT, *i.e.* a non-symmetry-breaking electronic and volume change, and a symmetry breaking ferroelastic transition, *i.e.* a change of a crystal system by a spontaneous shear strain. Hence, the dynamics of both volume and shear strain may contribute to trigger the ultrafast IMT. Here we investigate the prototypical Mott material V_2O_3, and discuss physical concepts underlying the dynamical strain wave pathway.

The mechanisms of generation and propagation of photoinduced strain waves in materials are known from the field of picosecond (ps) acoustics [9-13]. However, coupling such strain waves with electronic phase transitions, like IMT in Mott materials, poses an altogether new difficulty [7,14]. Namely, the conventional ps acoustics focuses on laser heating of external metallic transducers generating a longitudinal tensile strain wave in a material. Here, by contrast, internal compressive and shear stresses are generated by ultrafast electronic photoexcitation of the insulating phase, launching self-supported strain waves from free surfaces. In this regard, sample morphology affects the dynamical strain response [12,15] and by that the efficiency of strain dynamics on the ultrafast IMT. The relevance of vanadium sesquioxide V_2O_3 for exploring this new route stems from its phase diagram at thermal equilibrium (Fig.1a), considered as generic for Mott physics [16]. A first order IMT line separates two isosymmetric paramagnetic phases, PI and PM, with the same rhombohedral space group. Another first-order IMT, between AFI and PM phases, is coupled to antiferromagnetic and monoclinic symmetry breaking. The loss of threefold symmetry leads to the formation of ferroelastic domains in the AFI phase [17]. The AFI-PM transition is associated with -1.4% volume contraction. Volume and ferroelastic deformations therefore play a conspicuous role in IMT at thermal equilibrium and a central question is how this is reflected in the ultrafast dynamics of IMT.

Different studies have reported ultrafast photoinduced dynamics related with IMT in insulating phases of V_2O_3 by a near-IR pump (1.55 eV) on single crystal [18] or epitaxial films [19-21]. It is reported in Ref. [18] that transient state results from the excitation of electrons on bonding a_{1g} orbital, stabilized by atomic displacements associated with a totally symmetric A_g optical coherent phonon. In Refs. [19-21], the

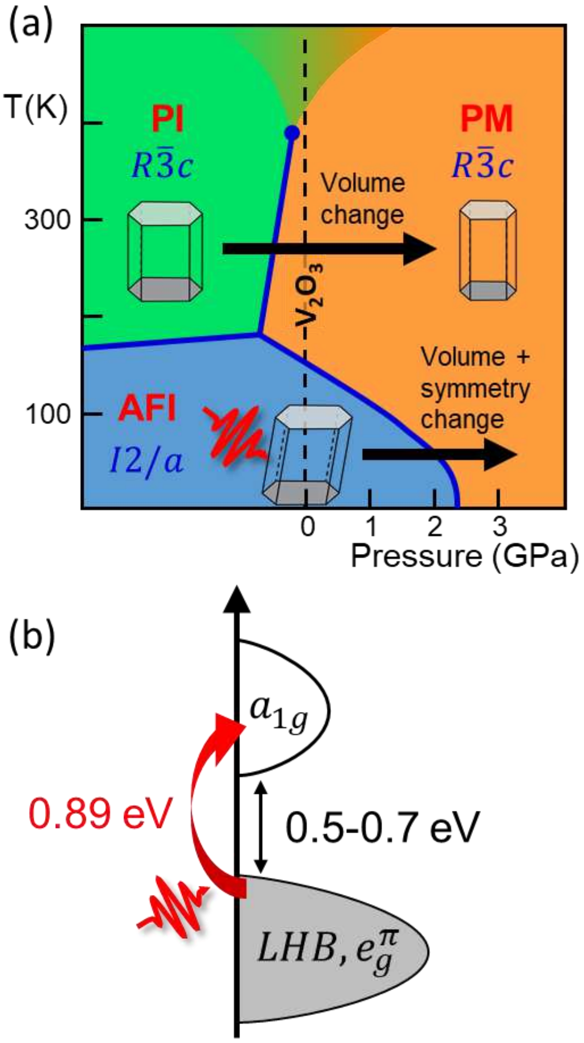

Fig.1 | **Phase Diagram and electronic bandstructure of V_2O_3. (a)** Unit cell symmetry and volume of three phases labelled PI, PM and AFI at thermodynamic equilibrium. Dashed line (vacuum or atmospheric pressure, see text), with cryogenic cooling down to 10 K, for experimental conditions used in this work, *i.e.* far from the AFI-PM transition line. Black arrows underline different nature of transitions, with the isosymmetric PI-to-PM involving only volume change, and the AFI-to-PM involving a fully symmetric volume change, as well as symmetry-breaking structural (ferroelastic to paraelastic) with magnetic changes. **(b)** Schematic representation of DOS in AFI phase; pump laser 0.89 eV close to the bandgap (0.5-0.7 eV) between Lower Hubbard Band (LHB) and the a_{1g} conduction band.

photoinduced AFI-to-PM dynamics observed close to coexistence regime is discussed in terms ultrafast laser heating and nucleation-growth based on concepts rooted in thermal kinetics of phase transition and questionably generalized to non-equilibrium ultrafast dynamics. In addition, the observations reported in Refs. [17,21] show a more complex dynamics influenced by the ferroelastic nanotexturing. Finally, intense THz pump pulse is able to induce an ultrafast pure electronic switching by quantum tunneling, but a slower thermal evolution is observed upon approaching the AFI-PM transition temperature [22]. The results presented here combine time-resolved (tr) transient reflectivity probing IMT electronic change, and X-ray diffraction (XRD) probing structural dynamics starting from the AFI phase. The chosen experimental conditions limit heating effects with a pump photon energy of 0.89 eV (Fig.1b) close to the optical gap [23-25], as well a base temperature below the AFI-PM coexistence regime to avoid heterogeneous nucleation. The results introduce a radically different mechanism from nucleation-growth, where the IMT propagates at sound velocity in the wake of compressive strain wave. They also reveal the role of structural symmetry breaking by the propagation of reverse shear strain wave at the scale of each ferroelastic domain. Finally, we clarify the limits of such IMT mechanism by comparing the response of a single crystal and nanocrystalline thin film.

Photoinduced Complete IMT and Symmetry Breaking in Thin Film

We probe the electronic component of photoinduced IMT by the change in reflectivity of a 116 nm thick granular film, with a grain size of about 40 nm, 300 ps after photoexcitation and at high fluence (Fig.2a,b and Extended Data Fig.1). It covers a broad spectral range, down to the low energies particularly sensitive to metallic state. The photoinduced spectral response matches the differential change in the static reflectivity between the AFI and PM phases, indicating a complete transformation to the metallic phase in the film on this time scale upon strong-excitation. In contrast, the photoinduced response of a single crystal shown in Fig.2c,d is significantly lower than its steady state counterpart, regardless the polarisation of the pump and the probe (Extended Data Fig.2). The complete photoinduced phase transition observed in the thin film is fully confirmed by ultrafast X-ray diffraction obtained on thin films of a comparable (106 nm) and a larger (270 nm) thickness, at FemtoMAX for sub-ps time-resolution, and at ESRF for high Q-resolution (Methods). Fig.2e,f shows 1D XRD patterns after azimuthal integration of 2D images, measured at 10 K without and with photoexcitation at a fluence inducing complete IMT. Two very clear trends emerge, characterizing the structural transformation from monoclinic AFI phase ($I2/a$ space group) to corundum rhombohedral phase ($R\bar{3}c$ space group). On the one hand, a shift of $(hk0)_H$ Bragg peaks towards large Q is observed, readily visible for $(110)_H$ and $(300)_H$ peaks (we use hereafter the hexagonal notation for clarity, even after splitting of peaks in the monoclinic phase). This demonstrates a photoinduced transient crystalline state mainly compressed in the hexagonal (a_H,b_H) plane in agreement with the volume change at thermal AFI-to-PM phase transition [26] (Extended Data Fig.3). On the other hand, a strong redistribution of intensity occurs on several Bragg peaks, with a narrowing and intensity increase at hexagonal peak position. This corresponds to the disappearance of monoclinic distortion in the AFI phase, particularly evident in the $(116)_H$ Bragg peak, sensitive to ferroelastic shear. These structural changes appear clearly in higher Q-resolution ESRF data shown in Fig.2g-j, especially the merging of three monoclinic peaks into the hexagonal $(116)_H$. A refinement of XRD patterns of initial and completely transformed phases reveals a full volume contraction $\Delta V/V = -1.5$ %, consistent with that at thermal equilibrium, as well as a complete reverse symmetry breaking (Extended data Fig.3).

Threshold for the Macroscopic I-to-M Transition

The evolution of transient reflectivity $\Delta R/R$ with fluence for different time delays gives fundamental information on how the transformation occurs (Fig.3a). For time scales below 1 ps, the increase is quasi-linear in both the thin film and crystal, suggesting an ensemble of independent photoinduced phenomena. In contrast, the thin film shows a non-linear response after 1 ps with a clear threshold. The occurrence of threshold and

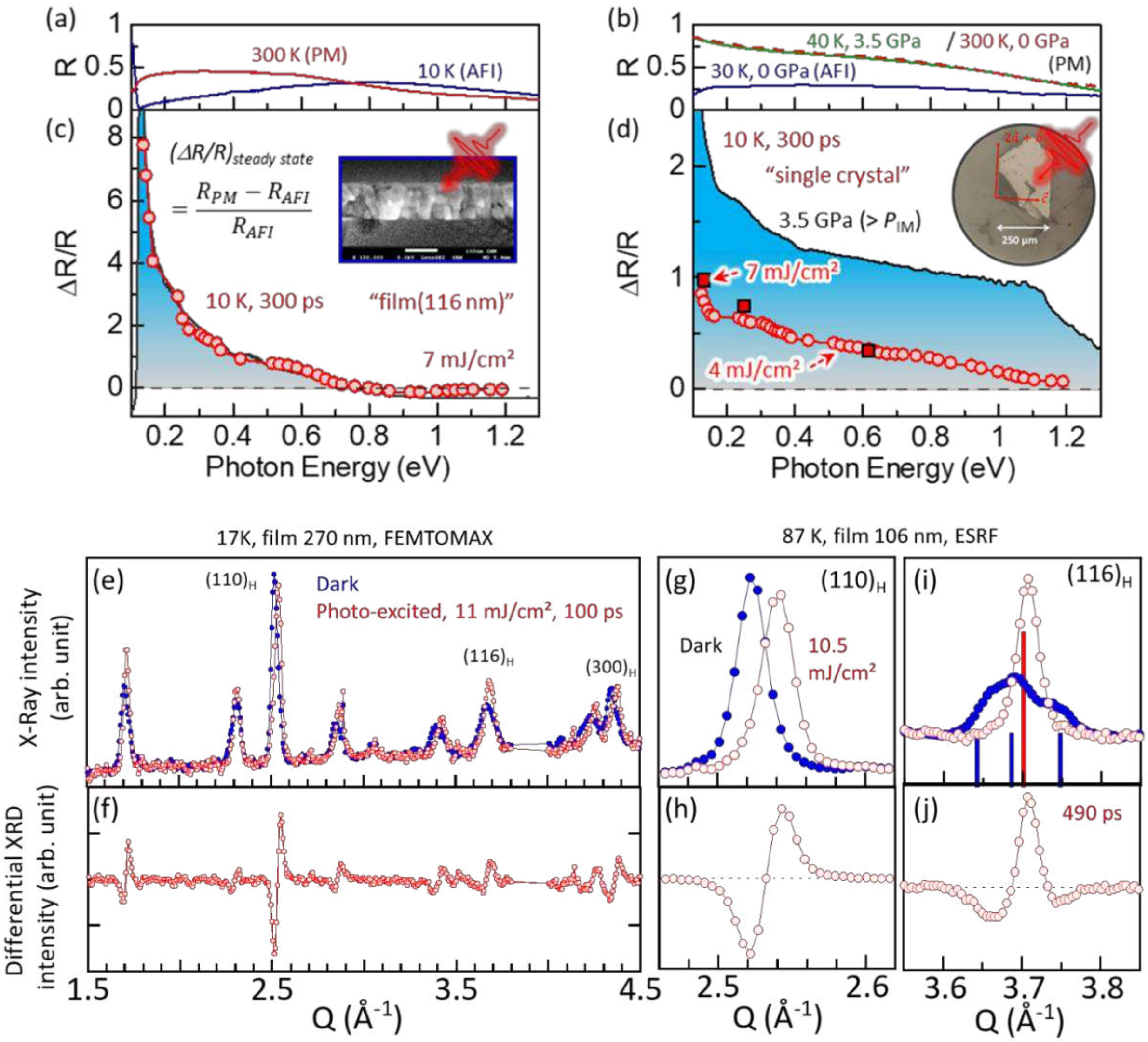

Fig. 2 | Evidence of a complete photoinduced I-to-M phase transition in V_2O_3 granular film and lack thereof in a single crystal. (a) Reflectivity of PM and AFI phases at thermal equilibrium measured on the 116 nm V_2O_3 film. **(c)** Relative difference $\frac{\Delta R}{R} = \frac{R_{PM}-R_{AFI}}{R_{AFI}}$ (blue shaded area) compared to the transient reflectivity change at 300 ps (red dots) measured at 10K over a broad spectral range. No rescaling used, the match of transient reflectivity with that expected of fully converted PM phase is due to applied fluence. Inset: Scanning Electron Microscope cross section image of the film, the reference scale bar (white line) is 100 nm. **(b and d)** same as (**a** and **c**) but for single crystal shown in the inset. In addition, Fig.1b shows similarity between reflectivity at 40 K and 3.5 GPa with reflectivity at 300K and 0 GPa. Polarizations of pump and probe lights are respectively parallel to $2\vec{a}+\vec{b}$ and $\vec{c}$ directions shown in the inset. **(e)** Diffraction pattern of the 270 nm thick film of V_2O_3 at 17K in the ground (Dark) and excited states (100ps delay) with Miller indices on peaks discussed in the text. **(f)** differential of (e) to emphasize the magnitude of structural change with S/N achieved at Femtomax. **(g)** and **(i)** Bragg reflections $(110)_H$ and $(116)_H$ of the 106 nm thick film at 87 K, bearing predominantly information on volume contraction and symmetry change, respectively, upon AFI to PM transition as measured at ESRF with lower time resolution but improved Q-resolution compared to Femtomax. The peak width and intensity indicate no phase coexistence at 500 ps, and complete transition to PM phase (smaller volume, higher symmetry). Vertical bars in **(i)** are Bragg peak positions and intensities expected in the monoclinic (blue) and hexagonal (red) phases at 300 K. **(h)** and **(j)** differential of **(g)** and **(i)** to emphasize the magnitude of structural change with S/N achieved at ESRF.

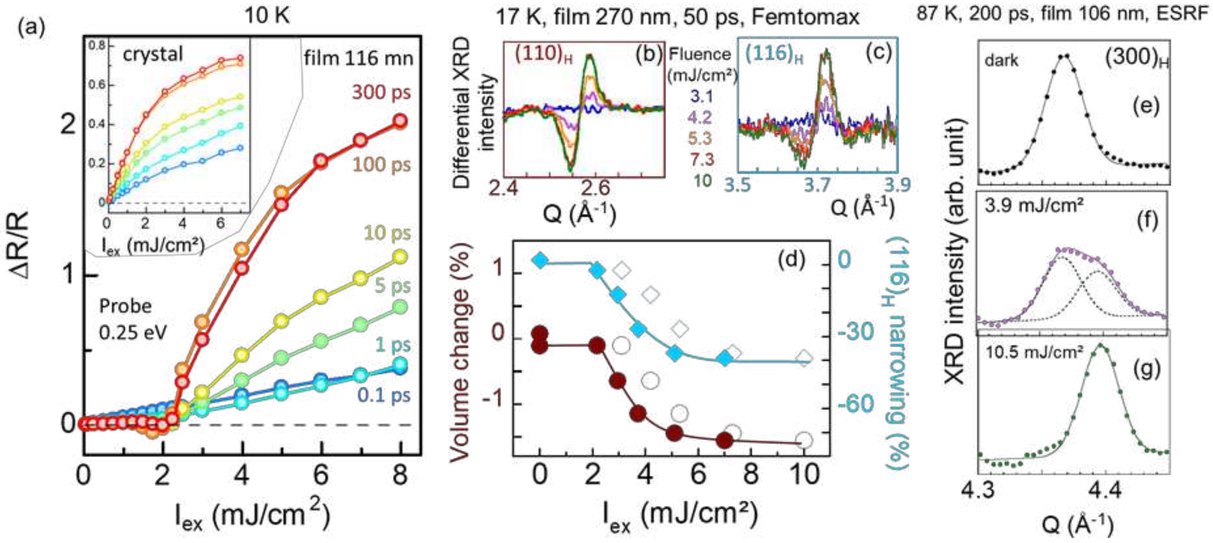

Fig. 3 | Impact of pump laser fluence on the photoinduced electronic and structural features of the I-to-M phase transition. (a) Pump (0.89 eV) laser fluence dependency of transient reflectivity measured at 10 K on a 116 nm V_2O_3 thin film at different delays, probed at 0.25 eV where electronic changes due metallization are most pronounced (Fig.2a). Fluence threshold for the apparent dynamics around around I_{ex} (excitation intensity) = 2 mJ/cm^2 and delays above 5 ps. Inset: fluence response of V_2O_3 single crystal showing no threshold. **(b)** and **(c)** time-resolved XRD differentials of $(110)_H$ and $(116)_H$ reflections bearing predominantly information on volume contraction and symmetry change, respectively, upon AFI to PM transition measured at 17 K and 50 ps after excitation at varying fluences. **(d)** Evolution with fluence of volume contraction, $(110)_H$ peak shift, and monoclinic to hexagonal symmetry change, $(116)_H$ peak narrowing. The threshold of 2 mJ/cm^2 and saturation around 8-10 mJ/cm^2 are very similar to the values seen in **(a)**. Open symbols correspond to applied laser fluences; filled symbols corrected for different pump incidence angle from **(a)**, see Methods. **(e-g)** Evolution of the $(300)_H$ peak illustrating the phase separation as function of fluence: dark AFI in black (dotted measured, solid fitted), high fluence PM in green (dotted measured, solid fitted), intermediate fluence with phase coexistence in purple (dotted measured, dashed lines AFI and PM peaks fitted).

amplified response ascertains a photoinduced macroscopic phase transition, as previously evidenced in different materials exhibiting isosymmetric part [6,27,28]. In contrast, the inset of Fig.3a does not reveal any threshold in single crystal. This supports the absence of photoinduced macroscopic IMT in single crystal, and rather suggests the coexistence of I and M states only at short length scales. The threshold for IMT in thin film is around 2 mJ/cm^2 at 10 K, and about 1 mJ/cm^2 at 100K (Extended Data Fig.4).

In addition, time-resolved XRD results shown in Fig.3b-g indicate that volume and shear changes take place also above a fluence threshold around 2 $mJ.cm^{-2}$. Moreover, in the 7-10 $mJ.cm^{-2}$ fluence range, tr-XRD unveil the previously discussed volume contraction of - 1.5 % and entire disappearance of monoclinic distortion, in agreement with the complete IMT probed by tr-reflectivity. This shows that the electronic change of the IMT follows the structural one. At intermediate fluence (3.9 $mJ.cm^{-2}$, see Fig.3f), the observation of distinct Bragg peaks of the initial and photoinduced phases indicates that the partially transformed state corresponds to a phase coexistence between PM an AFI phases at macroscopic scales.

Driving IMT by Photoinduced Strain Waves

The temporal signature of strain wave dynamics directly results from the propagation of photoinduced phase transformation on the acoustic time scale. Fig. 4a,b and Extended Data Fig. 5 show the evolution of the two structural changes, in two granular films of different thickness (106 and 270 nm) but similar grain size. Whereas the monoclinic → hexagonal transition is completed in less than 3 ps, the volume contraction requires longer time and shows the onset of around 9 ps. Unlike the dynamics of symmetry change, the time for volume contraction scales with the film thickness. Indeed, from the onset to the end of propagation, this time is 16 and 40 ps in the 106 and 270 nm films, respectively. These shear and volume dynamics can be rationalised with strain waves scenario: initial mechanical stresses with two components, a shear one in each ferroelastic domain, and a volumic one across the granular film. In both cases, the stored mechanical energy is relaxed by the propagation of a strain wave launched from interfaces under no net external stress. As the average size of ferroelastic domain is around 20 nm (see Extended Data Fig. 1b), we expect a propagation time of 2.5 ps at transverse acoustic velocity of 4 nm/ps [29-31] from the two opposite surfaces to the centre of the domain (Fig.5). Similarly, the expected propagation times for a longitudinal strain wave through the film at the reported acoustic velocity of 7-7.3 nm/ps [29-31] are 15 and 38 ps for the 106 and 270 nm, respectively, in agreement with the experimental values shown in Fig.4 for volume dynamics.

Remarkably, transient reflectivity follows closely the structural dynamics (Fig.4): a fast increase during the first ps is followed by a linear increase, concurrently with the propagation of the volume on the acoustic time scale. According to tr-XRD, V_2O_3 reaches the $R\bar{3}c$ symmetry after 3 ps with volume unchanged, hence resembling the PI phase shown in Fig.1. Since the PI phase has reflectivity greater than AFI [32], a fast reflectivity increase is expected on few ps. At longer delays, the dynamics of both tr-reflectivity and tr-XRD terminate in a long-lived electronic state of hundreds ps. A noteworthy feature is that the total duration of the dynamics is essentially the same regardless the laser fluence above the threshold. Moreover, the dynamics does not seem to vary between 10 K and 100 K. This reinforces the picture of a strain wave pathway, since the coherent wave propagation is in essence independent of temperature, at least outside of the phase coexistence regime close to the thermal IMT.

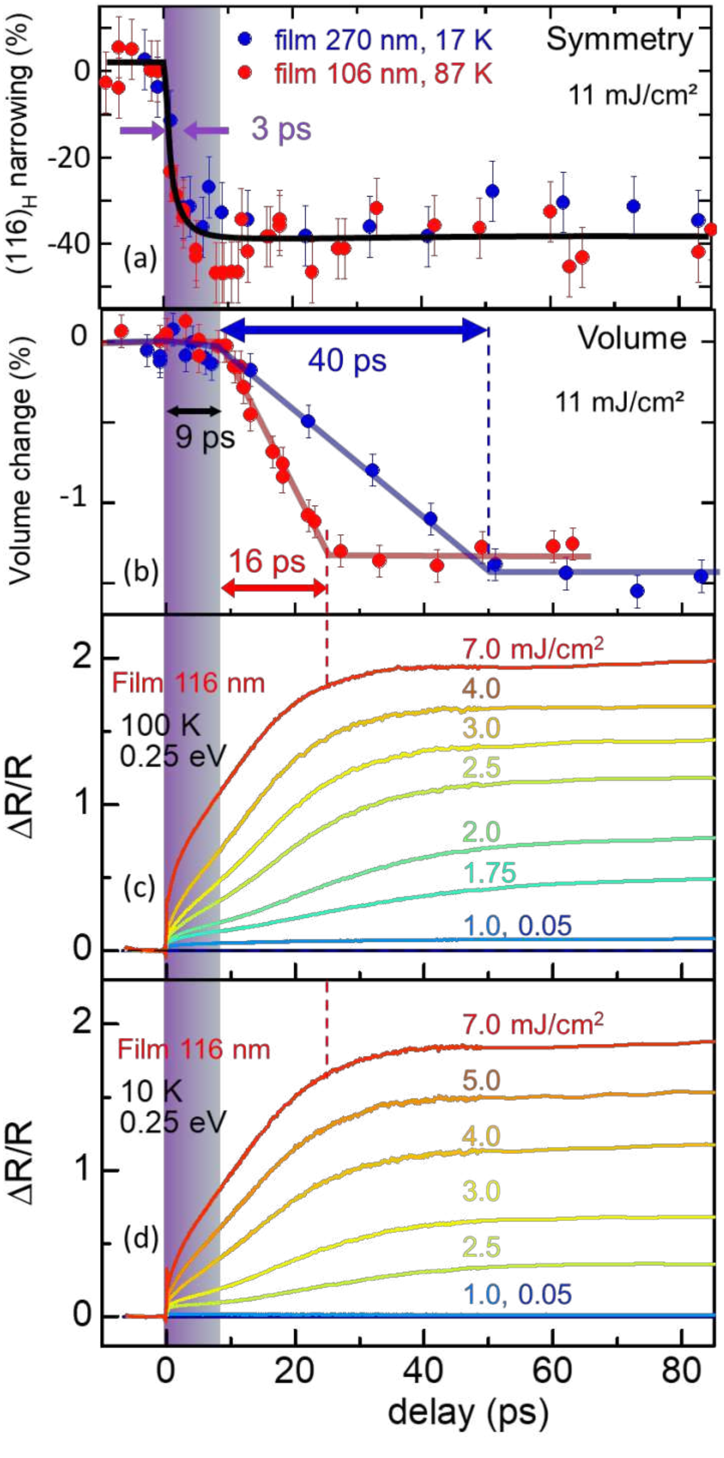

Fig. 4 | Structural and electronic changes on the acoustic time-scales. (a) Evolution of photoinduced symmetry change probed by $(116)_H$ peak narrowing in 106 nm (red) and 270 nm (blue) films at 87 K and 17 K, respectively. The signal rises in less than 3 ps, after time binning over 1 ps with jitter corrected. **(b)** Evolution of volume change probed by the $(110)_H$ Bragg peak shift (see Extended Data Fig.3). Apparent incubation time of 9 ps is followed by a linear rise of 16 ps for 106 nm, and 40 ps for 270 nm films. Colour coding as in (a), but time binning of 2 ps. **(c)** and **(d)** transient reflectivity of the 116 nm film excited with different fluences at 100K and 10K, respectively. The linear evolution of transient reflectivity coincides temporally with the onset of 9 ps seen in tr-XRD (shaded area) and the end of volume contraction 16 ps later (dashed red line).

Physical Picture and Outlook

The experimental results help unravel concepts to draw a general physical picture of the dynamical strain waves pathway in Mott materials (Fig.5), and photoinduced phase transitions at large.

Isosymmetric vs symmetry-breaking photoinduced transitions. Symmetry-breaking and isosymmetric phase transitions differ [33], and the question is how it manifests in photoinduced dynamics. At zero conjugated field, spontaneous symmetry-breaking leads to the formation of domains due to the loss of symmetry elements. A new length scale emerges in the material, namely the domain size. In contrast, an isosymmetric phase transition takes place between two homogeneous phases without new length scale. Consequently, the shear dynamics for reverse ferroelastic transition, scaling with the domain size, is faster than the volume dynamics scaling with the much larger film thickness, even though the shear propagates at smaller transverse acoustic velocity. Another point is how the totally symmetric volume strain $\Delta V/V$ and the symmetry-breaking strain φ couple to each other. Symmetry considerations impose a linear-quadratic coupling energy ~ $\Delta V/V.\varphi^2$ to determine the potential energy landscape. This type of coupling is generally used to discuss the volume strain induced by pure spontaneous ferroelastic deformation [34]. However, the role of volume in V_2O_3 is different since it is directly involved in the isosymmetric Mott transition coupled to the ferroelastic one. In fact the volume evolves independently from the shear only after the fast recovery of paraelastic state. A complete description of the coherent dynamics by time-dependent Ginzburg-Landau approaches, including the strain propagation and control by fluence and initial temperature, remains a theoretical challenge. Furthermore, the comparison with the case of VO_2 [35] where the ferroelastic deformation is dominant would be instructive in future. We also suspect that these dynamical concepts could be extended to any system exhibiting a *gas-liquid-solid*-like phase diagram [26,36].

Beyond conventional picosecond acoustics. In conventional ps acoustics, the thermal stress and subsequent tensile strain waves are generated by laser heating of metallic transducers. The situation differs in insulators, where long-lived photoexcited electronic states can persist after ultrafast intraband relaxation. This reduces lattice heating, especially for pump photon energy close to the optical gap, such as in our study. In addition, the lifetime of photoexcited electrons may be extended by local self-trapping [37] implying structural distortions of V_2O_3 units, such as small polarons [38]. This could be the situation in V_2O_3, since long-lived transient states are observed at low fluence (Extended data Fig.6). In order to recover mechanical equilibrium with the environment, both longitudinal and transverse shear strain waves are launched, leaving in their wake long lived crystal deformations: contracted volume and reduction of spontaneous shear (Fig.5). As stated in Ref.[13], this holds even for spatially homogeneous photoexcitation, contrary to the claim that only 2D in-plane growth must be considered [19]. This also differs from the effects of tensile strain wave externally launched at a complex-oxide heterointerface on the dynamics of electronic, magnetic and structural degrees of freedom [39]. Since shear forces cancel at the surface of each ferroelastic domain, it is straightforward that shear dynamics scales

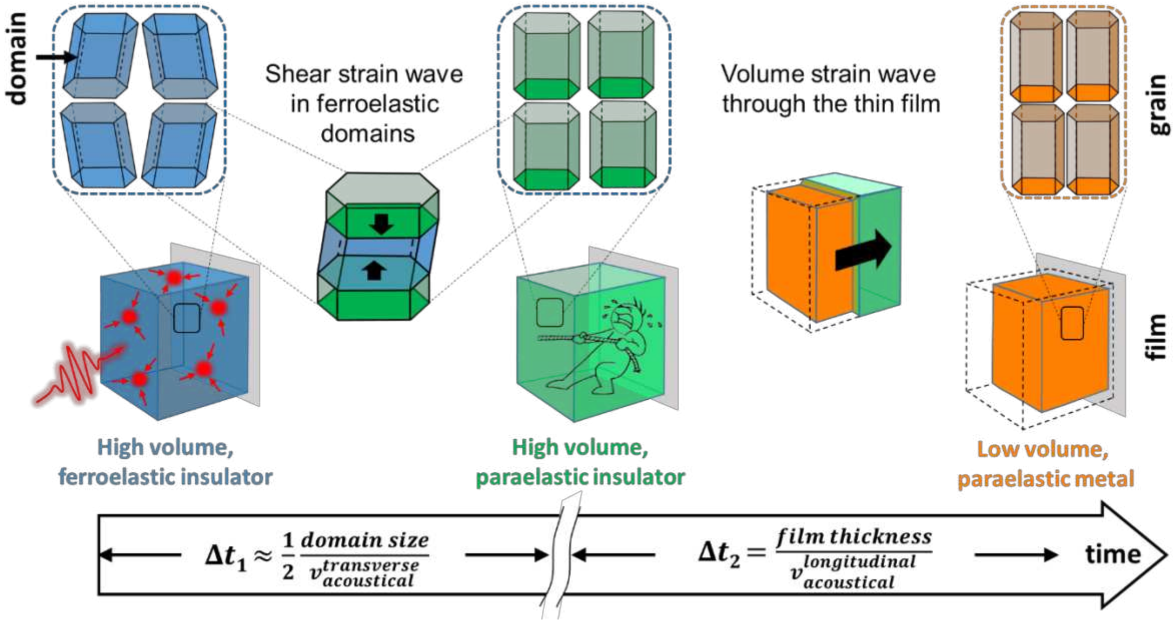

Fig. 5 | Schematic illustrating the photoinduced strain waves driving the AFI-to-PM transition in granular thin film of V_2O_3. Ultrafast laser pulse excites long-lived electronic precursors, leading to fast build-up of shear and volume mechanical stress. At first, the stress is relaxed by launching a shear strain wave within each ferroelastic domain of the granular film, Δt_1. A compressive volume strain wave propagates from free surface of the film towards the substrate, leaving in its wake the insulator to metal transition, Δt_2.

with the domain size. We note that the ultrafast time scale for recovery of paraelastic state is consistent with the existence of a few domains in each grain. Moreover, since the magnetic structure in the honeycomb plane and the monoclinic distorsion interplay [40], it is likely that the inverse ferroelastic transition favour a concomitant antiferromagnetic to paramagnetic transition. Our study also unveiled an intriguing feature, the observation of a delayed onset for the volume dynamics. At this stage it is difficult to give a satisfying explanation. We may only mention a possible relation with the granular nature of thin film, known to affect the longitudinal strain response [12,15,41], as well as the coupling between volume and shear strains slowing down the initial volume dynamics [42]. Another feature is the absence of complete transformation in the single crystal which is consistent with a strain wave picture. Single crystal indeed constitutes a continuous medium where transient longitudinal deformations occur only in the direction perpendicular to the surface, because of in-plane lateral clamping [12,15]. This situation is avoided in granular film, where the volume of each grain is essentially free to deform in all directions. This hints at difficulties to interpret the results on epitaxial films, also submitted to the effects of domain nanostructuring and coexistence between AFI and PM phases. Finally, the observation of the macroscopic IMT in the absence of any strain oscillation due to wave reflection at interfaces with air and substrate, in contrast with a homogeneous phase [43], points out another difference with conventional ps acoustics.

Central role of volume contraction in IMT. Our results highlight the active role of volume contraction for the transformation from I-to-M electronic state at a macroscopic scale. For a given volume, the evolution from I-to-M macroscopic state implies only electronic reorganization and small atomic displacements in the unit cell. Therefore, it quasi-instantaneously follows the propagation of volume change, unlike in systems where the local dynamics is governed by slow thermal activation [44]. From this viewpoint, thin films of transition metal oxides hold promise for ultrafast switching of functional properties, with operation speed limited by the sound velocity. Moreover, the observation of a threshold proves the existence of a critical value of electronic excitation which triggers the self-amplification of IMT at macroscopic scale. This change of scale from local to macroscopic manifests also by a loss of coherence of in-phase optical phonons [45]. A theoretical study on V_2O_3, based on a two orbital model, shows that the excess population of electrons in the upper orbital and holes in lower orbital may lead to a gap collapse above a threshold [46]. The more the excess population increases, the more the effective gap decreases. Importantly, long range elastic interactions play a role too in stimulating cooperative response. As a matter of fact, compressive stresses lead to an effective positive chemical pressure [47]. When the density of excited electrons increases, the chemical pressure increases proportionally, *i.e.* as an internal mean field inducing positive feedback. Hence the volume contraction reinforces the cooperativity synergetically with electronic Mott Physics, both related with the same isosymmetric order parameter. Furthermore, the decrease of fluence threshold with at higher base temperature agrees with reduced distance to phase transition line. It should be emphasised that many considerations about coherent strain dynamics and cooperative feedback remain relevant even for lattice heating.

To conclude, this work establishes that the IMT can emerge only when the volume is dynamically contracted. It also clarifies the respective role of shear and volume strain wave dynamics for this transformation. It highlights the difference with conventional ps acoustics, and the crucial role of the sample morphology. Finally, we expect that the physical picture summarized in Fig.5 goes beyond the specific case of V_2O_3, and can be applied in many quantum materials with phase transitions involving elastic deformations [48]. This could also guide the assessment of the ultimate performance of ultrafast devices based on Mott insulators [49,50]

References:

1 Huber, T. et al. Coherent structural dynamics of a prototypical charge-density-wave-to-metal transition, *Physical Review Letters* **113**, 026401 (2014). doi: 10.1103/PhysRevLett.113.026401

2 Teitelbaum, S. W. et al. Real-time observation of a coherent lattice transf Physical Review Bormation into a high-symmetry phase, *Physical Review X* **5**, 031081 (2018). doi: 10.1103/PhysRevX.8.031081

3 Trigo, M. et al. Coherent order parameter dynamics in $SmTe_3$ *Physical Review B* **99**, 104111 (2019). doi: 10.1103/PhysRevB.99.104111

4 Basov, D. N., Averitt, R. D. & Hsieh, D. Towards properties on demand in quantum materials, *Nature Materials* **6**, 1077 (2017). doi: 10.1038/nmat5017

5 De la Torre, A., et al. Nonthermal pathways to ultrafast control in quantum materials *Reviews of Modern Physics* **93**, 041002 (2021). doi: 10.1103/RevModPhys.93.041002

6 Bertoni, R. et al. Elastically driven cooperative response of a molecular material impacted by a laser pulse, *Nature Materials* **15**, 606 (2016). doi: 10.1038/nmat4606

7 Mariette, C. et al. Strain wave pathway to semiconductor-to-metal transition revealed by time-resolved X-ray powder diffraction, *Nature Communications* **12**, 1239 (2021). doi: 10.1038/s41467-021-21316-y

8 Verma, A. et al. Picosecond volume expansion drives a later-time insulator-metal transition in a nano-Textured Mott insulator, http://arxiv.org/abs/2304.02149. doi: 10.48550/arXiv.2304.02149

9 Thomsen, C., Grahn, H. T., Maris, H.J. & Tauc, J. Surface generation and detection of phonons by picosecond light pulse, *Physical Review B* **34**, 4129 (1986). doi: 10.1103/PhysRevB.34.4129

10 Matsuda, O., Larciprete, M. C., Li Voti, R. & Wright, O. B. Fundamentals of picosecond laser ultrasonics *Ultrasonics* **56**, 3 (2015). doi: 10.1016/j.ultras.2014.06.005

11 Ruello, P. & Gusev, V. E. Physical mechanisms of coherent acoustic phonons generation by ultrafast laser action *Ultrasonics* **56**, 21 (2015). doi: 10.1016/j.ultras.2014.06.004

12 Mattern, M. et al. Concepts and use cases for picosecond ultrasonics by x-rays Photoacoustics 31, 100503 (2023). doi: 10.1016/j.pacs.2023.100503

13 Schick, D. et al. Ultrafast lattice response of photoexcited thin films studied by X-ray diffraction *Structural Dynamics* **1**, 064501 (2014). doi: 10.1063/1.4901228

14 Okimoto, Y. et al. Ultrasonic propagation of metallic domain in $Pr_{0.5}Ca_{0.5}CoO_3$ undergoing a photoinduced Insulator-to-Metal Transition *Physical Review Letters* **103**, 027402 (2009). doi: 10.1103/PhysRevLett.103.027402

15 Von Reppert, A. et al. Ultrafast laser generated strain in granular and continuous FePt thin films *Applied Physics Letters* **113**, 123101 (2018). doi: 10.1063/1.5050234

16 McWhan, D. B. et al. Electronic specific heat of metallic Ti-doped V2O3 *Physical Review Letters* **27**, 941 (1971). doi; 10.1103/PhysRevLett.27.941

17 Ronchi, A. et al. Nanoscale self-organization and metastable metallicity in Mott insulators *Nature Communications* **13**, 3730 (2022). doi: 10.1038/s41467-022-31298-0

18 Lanz, G. et al. Ultrafast evolution and transient phases of prototype out-of-equilibrium Mott-Hubbard material *Nature Communications* **8**, 13917 (2017). doi: 10.1038/ncomms13917

19 Abreu, E. et al. Dynamic conductivity scaling in photoexcited V_2O_3 Thin Films, *Physical Review B* **92**, 085130 (2015). doi: 10.1103/PhysRevB.92.085130

20 Singer, A. et al. Nonequilibrium phase precursors during a photoexcited insulator-to-metal transition in V_2O_3 *Physical Review Letters* **120**, 207601 (2018). doi: 10.1103/PhysRevLett.120.207601

21 Ronchi, A. et al. Early-stage dynamics of metallic droplets embedded in nanotextured Mott insulating phase of V_2O_3, *Physical Review B* **100**, 075111 (2019). doi: 10.1103/PhysRevB.100.075111

22 Giorgianni, F. et al. Overcoming the thermal regime for the electric-field driven Mott transition in vanadium sesquioxyde, *Nature Communications* **10**, 1159 (2019). doi: 10.1038/s41467-019-09137-6

23 Thomas, G. A. et al. Observation of the gap and kinetic energy in a correlated insulator *Physical Review Letters* **73**, 1529 (1994). doi: 10.1103/PhysRevLett.73.1529

24 Baldassare, L. et al. Quasiparticle evolution and pseudogap formation in V_2O_3: an infrared spectroscopy study *Physical Review B* **77**, 113107 (2008). doi: 10.1103/PhysRevB.77.113107

25 Stewart, M. K. et al. Insulator-to-metal transition and correlated metallic state of V_2O_3 investigated by optical spectroscopy *Physical Review B* **85**, 205113 (2012). doi: 10.1103/PhysRevB.85.205113

26 McWhan, D. B. & Remeika, J. P. Metal-Insulator transition in $(V_{1-x}Cr_x)_2O_3$ *Physical Review B* **2**, 3734 (1970). doi: 10.1103/PhysRevB.2.3734

27 Okamoto, H. et al. Photoinduced phase transition in tetrathiafulvalene-p-chloranil in femtosecond reflection spectroscopy *Physical Review B* **70**, 165202 (2004). doi: 10.1103/PhysRevB.70.165202

28 Wall, S. et al. Ultrafast disordering of vanadium dimers of photoexcited VO_2 *Science* **362**, 572 (2018). doi: 10.1126/science.aau3873

29 Motin Seikh, Md. et al. A Brillouin study of the temperature-dependences of the acoustic modes across the insulator-metal transitions in V_2O_3 and Cr-doped V_2O_3 *Solid State Communications* **138**, 466 (2006). doi: 10.1016/j.ssc.2006.03.026

30 Yelon, W. B. & Keem, J. E. The elastic constants of V_2O_3 in the insulating phase *Solid State Communications* **29**, 775 (1979). doi: 10.1016/0038-1098(79)90159-5

31 Yethiraj, M., Werner, S.A., Yelon, W.B. & Honig, J. M. Phonon anomalies and the magnetic transition in pure and Cr-doped V_2O_3 *Physical Review B* **36**, 8675 (1987). doi: 10.1103/PhysRevB.36.8675

32 Lo Vecchio, I. et al. Optical properties of V_2O_3 in its whole phase diagram *Physical Review B* **91**, 155133 (2015). doi: 10.1103/PhysRevB.91.155133

33 Chaikin, P. M. & Lubensky, T. C. *Principles of condensed matter physics*, (Cambridge University Press, 1995)

34 Carpenter, M. A., Salje, E. K. H. & Graeme-Barber A. Spontaneous strain as a determinant of thermodynamic properties for phase transitions in minerals *European Journal of Mineralogy* **10**, 621 (1998). doi: 10.1127/ejm/10/4/0621

35 Pouget, J. P. Basic aspects of the metal-insulator transition in vanadium dioxide VO_2: a critical review *Comptes Rendus Physique* **22**, 37 (2021). doi: 10.5802/crphys.74

36 Buron-Le cointe, M. et al. Back to the structural and dynamical properties of neutral-ionic phase transitions *Crystals* **7**, 285 (2017). doi: 10.3390/cryst7100285

37 Nasu, K. Real time quantum dynamics of spontaneous translational symmetry breaking in the early stage of photo-induced structural phase transitions *Applied Science* **8**, 332 (2018). doi: 10.3390/app8030332

38 Wickramane, D., Bernstein, N. & Mazin, I. I. Role of defects in the metal-insulator transition in VO_2 and V_2O_3 *Physical Review B* **99**, 214103 (2019). doi: 10.1103/PhysRevB.99.214103

39 Först, M. et al. Multiple supersonic phase fronts launched at a complex-oxide heterostructures *Physical Review Letters* **118**, 027401 (2017). doi: 10.1103/PhysRevLett.118.027401

40 Grieger, D. & Fabrizio, M. Low-temperature magnetic ordering and structural distortions in vanadium sesquioxide V_2O_3 *Physical Review B* **92**, 075121 (2015). doi: 10.1103/PhysRevB.92.075121

41 Reid, A.H. et al. Beyond a phenomenological description of magnetoscriction *Nature Communications* **9**, 388 (2018). doi: 10.1038/s41467-017-02730-7

42 Li, J. et al. Probing the pathway of an ultrafast structural phase transition to illuminate the transition mechanism in Cu_2S *Applied Physics Letters* **113**, 041904 (2018). doi: 10.1063/1.5032132

43 Huitric, G. et al. Impact of the terahertz and optical pump penetration depths on generated strain waves temporal profiles in a V2O3 thin film *Faraday Discussions* **237**, 389 (2022). doi: 10.1039/D2FD00013J

44 Volte, A. et al. Dynamical limits for the molecular switching in a photoexcited material revealed by x-ray diffraction *Communications Physics* **5**, 16_ (2022). doi: 10.1038/s42005-022-00940-0

45 Johnson, A.S. et al. Ultrafast loss of lattice coherence in the light-induced structural phase transition of V_2O_3 *Physical Review Letters* **129** 255701 (2022). doi: 10.1103/PhysRevLett.129.255701

46 Sandri, M. & Fabrizio, M. Nonequilibrium gap collapse near a first-order Mott transition *Physical Review B* **91**, 115102 (2015). doi: 10.1103/PhysRevB.91.115102

47 Spiering, H., Boukheddaden, K., Linares, J. & Varret, F. Total free energy of a spin-crossover molecular system Physical Review B **70**, 184106 (2004). doi: 10.1103/PhysRevB.70.184106

48 Guzman-Verri, G.G, Brierley, R. T. & Littlewood, P. B. Cooperative elastic fluctuations provide tuning of the metal-insulator transition *Nature* **576**, 429 (2019). doi: 10.1038/s41586-019-1824-9

49 Sood, A. et al. Universal phase dynamics in VO_2 switches revealed by ultrafast operando diffraction *Science* **373**, 352 (2021). doi: 10.1126/science.abc0652

50 Cario, L., Tranchant, J., Corraze, B. & Janod, E. Chapter 10 - Correlated transition metal oxides and chalcogenides for Mott memories and neuromorphic applications. in *Metal Oxides for Non-volatile Memory* (eds. Dimitrakis, P., Valov, I. & Tappertzhofen, S.) 307–360 (Elsevier, 2022). doi: 10.1016/B978-0-12-814629-3.00010-6.

Methods

Materials synthesis and characterization

V_2O_3 single crystals were obtained by introducing 500 mg of V_2O_3 powder - previously prepared by reducing V_2O_5 (Aldrich, >99.6%) at 900 °C for 10 h under a Ar 95% / H_2 5% gas flow - in a silica tube, along with 40 mg of sulfur as a vapor phase transport agent. The tube was vacuum sealed, heated up to 1050 °C in a temperature gradient (≈10 °C/cm) furnace, and then cooled down at −2 °C/h to 900 °C, before a faster cooling (−300 °C/h) to room temperature. This treatment resulted in a high yield of V_2O_3 single crystals of typical size 300-500 µm.

Thin film of V_2O_3 were deposited by reactive sputtering of V targets in Ar 95% / O_2 5% discharge [51] on (0001)-oriented sapphire substrates. Post deposition annealing at 530°C in a reducing Ar 95 % / H_2 5% gas flow yields a granular, polycrystalline and single-phased V_2O_3 film, as evidenced in Extended Data Fig. 1. The typical domain size, estimated by analyzing the width of X-ray diffraction Bragg peaks with the Scherrer formula gives 40 nm at room temperature in the hexagonal $R\bar{3}c$ phase and 20 ± 5 nm at 87 K in the monoclinic $I2/a$ phase. The domain size at room temperature is consistent with the average grain size observed by Scanning Electron Microscopy (Extended Data Fig. 1). The significant decrease of the domains size in the monoclinic phase indicates that each single-domain grain at room temperature splits on average into a few domains at the hexagonal $\overline{R3}c$ to monoclinic $I2/a$ transition.

Resistivity *vs* temperature curves displayed in Extended Data Fig. 1d allow detecting typical insulator to metal transition temperatures around 160 K upon heating in the single crystal, as expected for stoichiometric V_2O_3 [25]. Transition temperature above 135 K involving a 10^5 increase of resistivity in the films indicate a composition very close to stoichiometry.

Finally, let us mention that evaluating in a reliable way the penetration depth at 0.89 eV of the pump laser used in this study is not an easy task. Estimates based on published data on reflectivity [32,52,53] or ellipsometry data [54] leads to penetration depths at 0.89 eV varying between 150 nm [54] and 800 nm [52]. Our own measurements, evaluated from the reflectivity and transmittance of thin films in the AFI phase, give a slightly narrower estimate, in the 200-400 nm range. This ensures a substantial photoexcitation of the V_2O_3 films used in this work (thickness from 100 nm to 270 nm) up to the substrate.

Transient reflectivity measurements

For optical pump-probe spectroscopy for measuring transient reflectivity (ΔR/R) spectra, the fundamental output from a Ti: Sapphire regenerative amplifier, operating at 1 kHz, 800 nm, with a pulse width of *ca*. 100 fs, was used for the excitation of optical parametric amplifiers (OPAs). Wavelength of an OPA for pump beam was set at 1400 nm (0.89 eV), whereas another OPA is used for probe beam covering the spectral range between 1000 -12000 nm (0.1 -1.2 eV). The probe beam was focused on the center of the pumping area on the sample which is set in the conduction-type liquid-He cryostat. Polarization directions of pump and probe beams are normal to each other.The diameters of pumping and probing areas are 400-500 micron and 100-200 micron, respectively. Then the reflected beam from the sample was detected by an InGaAs (1000-2200 nm) or a HgCdTe (2500-10000 nm) photodetector after passing through a monochromator. The pump-on and pump-off were alternately switched by the feed-back-controlled optical chopper, synchronized with the 1 kHz laser driver. Each probe shot was sampled using boxcar integrators. After normalization by a reference pulse, the observed intensity of respective shots was recorded in the PC to calculate $\Delta R/R$. Time resolution is 150-200 fs depending on the probing wavelength.

Ultrafast X-ray diffraction

1- FEMTOMAX

Experimental set-up

The sub-picosecond time-resolved X-Ray diffraction experiment was carried out at the FemtoMAX beamline at MAX IV Laboratory in Sweden. The sample was placed in the GIXS[i] endstation operated at ultrahigh vacuum $< 10^{-7}$ mbar and equipped with the JANIS ST-400 UHV supertran cryostat allowing for a broad temperature range (10 – 500 K) of sample temperatures. The sample temperature was monitored using a DT-670B silicon diode mounted next to a sample and a standard temperature controller (Model 335) from the Lake Shore Cryotronics, Inc. 100 fs long X-ray pulses delivered at 10 Hz with tunable energy around 9 keV was used for the experiment. A double multilayer monochromator with the 2 % bandwidth delivered by Rigaku was used to select the X-ray energy. The X-ray spot size on sample, tilted by 6 deg from grazing incidence, was 60×570 μm^2 (FWHM). X-ray scattering was carried out in a forward geometry. X-rays scattered from the V_2O_3 sample were collected using a Pilatus time over threshold detector from Dectris, mounted at a distance of 12 cm from the sample at an angle of 30º. The highest scattering vector giving acceptable resolution was $Q = 4.5$ $Å^{-1}$.

Laser system and synchronisation

The 1300 nm central wavelength laser pump pulse was generated from in an OPA (HE-TOPAS, Light Conversion). The beam was incident on the sample at an angle of 23 degrees relative to the sample surface with either s-polarization (yielding a reflecticity at the film surface $R \approx 0.5$) or p-polarization ($R \approx 0$). The footprint was 300 µm (FWHM, lateral) and 2.8 mm (FWHM, longitudinal). The maximum peak fluence under these conditions was 60 mJ/cm^2. As only 50 % of incident fluences measured with s-polarization is transmitted to the film, such as in Fig.2d, the tr-XRD fluences need to be rescaled by a factor of ≈ 0.70 to be compared with transient reflectivity ones obtained in normal incidence with 75 % of incident light transmitted to the film. The synchronization between the laser and x-ray pulse was managed by electronically phase locking the Ti:Sapphire mode-locked laser, to the reference RF signal, used in the LINAC, utilizing a standard locking scheme. Pump/probe jitter and drifts of each shot was recorded using a monitor developed at the FemtoMAX beamline. This pump/probe delay monitor extracts its reading from signals derived from a fast photo diode, for the laser pulse, and a pickup antenna at the electron bunch transport tube after the FemtoMAX undulator pair. The two signals are combined and in turn excites a broadband RF cavity band pass filter. The resulting ringing signal pair is digitally sampled and processed by an algorithm that extracts the delay from the relative phases of the signal pair. The accuracy of this pump/probe delay monitor has been tested to be 210 fs (FWHM).

2- ESRF

X-ray diffraction experiment at ESRF, ID09 beamline, was performed during hybrid mode (24x8 multiple electron bunches + 1 single bunch). The single electron bunch (8 mA) was used in the experiment. The ID09 setup was discussed in detail previously [55]. Briefly, a fast rotating chopper was used to isolate X-ray single pulses (each < 100 ps long) at 1 KHz repetition rate. The X-rays energy was centered at 15 keV. Cryogenically cooled Si(111) monochromator was used to reduce the x-ray bandwidth ($\Delta E/E = 10^{-4}$) in order to optimize the Q-resolution. The measurements were taken in reflection geometry with a fixed incident angle of 6 degrees. In this geometry, the X-ray footprint on the sample was 50 (horizontal) × 250 (vertical) μm^2. Diffracted images were collected on a Rayonix MX170-HS CCD detector (sample to detector distance = 150 mm).

A synchronized Ti:Sapphire laser with 1.5 ps pulse duration was used to photo-excite the sample. The 1300 nm pump wavelength was obtained using an OPA (TOPAS, LightConversion). Laser was hitting the sample from the top, perpendicular to x-rays, and focused to accommodate the elongated x-ray footprint. Spot size on sample was 1.17 mm (along x-ray direction) * 0.33 mm.

Measurements were taken in stroboscopic mode and each image was recorded with 10^3 shots exposures. “Negative” delays, for which x-ray arrive before photo-excitation, were interleaved as references. The delay sequences were repeated several times to increase the signal to noise ratio on differential patterns.

The sample was mounted on the cold finger of a specially designed continuous N_2-flow cryostat with Mylar windows for transmission of incident and diffracted 15 keV x-rays, and a UV-fused silica window for pump laser transmission.

Reflectivity under pressure

Low temperature pressure-dependent optical conductivity spectra have been deduced from nearly normal incidence sample-diamond reflectivity $R_{sd}(\omega)$ between 550 and 12 000 cm^{-1} wave numbers (8066 cm^{-1} = 1 eV) on a 100 x 100 μm^2 single crystal up to 3.5 GPa using a BETSA membrane diamond anvil cell. A closed cycle cryostat was used to cool down the sample. The sample was loaded inside a stainless-steel gasket hole together with KBr as a hydrostatic medium. The gasket was used as a reference mirror. $R_{sd}(\omega)$ was measured by using a homemade high-vacuum microscope including an X15 Schwarzchild objective connected to a BRUKER IFS 66v/S Fourier Transform Spectrometer with a Mercury-Cadmium-Telluride detector and thermal light sources. Pressure was measured with the standard ruby fluorescence technique. Measurements were performed at fixed temperature (40 K) by increasing the pressure. To obtain the optical conductivity from the $R_{sd}(\omega)$, we used the variational dielectric function method [56].

Data availability

Data sets generated during the current study are available from the corresponding authors on reasonable request.

References

[51] Querré, M. *et al.* Non-volatile resistive switching in the Mott insulator $(V_{1-x}Cr_x)_2O_3$. *Physica B: Condensed Matter* **536**, 327–330 (2018). doi: 10.1016/j.physb.2017.10.060

[52] Thomas, G. A. *et al.* Observation of the Gap and Kinetic Energy in a Correlated Insulator. *Phys. Rev. Lett.* **73**, 1529–1532 (1994). doi: 10.1103/PhysRevLett.73.1529

[53] Baldassarre, L. *et al.* Quasiparticle evolution and pseudogap formation in V_2O_3: An infrared spectroscopy study. *Phys. Rev. B* **77**, 113107 (2008). doi: 10.1103/PhysRevB.77.113107

[54] Stewart, M. K. *et al.* Insulator-to-metal transition and correlated metallic state of V_2O_3 investigated by optical spectroscopy. *Phys. Rev. B* **85**, 205113 (2012). doi: 10.1103/PhysRevB.85.205113

[55] Cammarata, M. *et al.* Chopper system for time resolved experiments with synchrotron radiation. *Review of Scientific Instruments* **80**, 015101 (2009). doi: 10.1063/1.3036983

[56] A. B. Kuzmenko, Kramers-Kronig constrained variational analysis of optical spectra, Rev. Sci. Instrum. 76, 083108 (2005). doi: 10.1063/1.1979470

Acknowledgements

M.Lo. gratefully acknowledges the Agence Nationale de la Recherche for financial support under grants ANR-16-CE30-0018 (“Elastica”) and ANR-19-CE29- (“Multicross“). The authors thank Nicolas Stephant for this help on Scanning Electron Microscopy experiments. We acknowledge the European Synchrotron Radiation Facility (ESRF) for provision of synchrotron radiation facilities and use of beamline ID09, and thank R. Garlet, B. Richer and Y. Watier for their help in setting up the cryo cooling system. S.I. acknowledges JST CREST (JPMJCR1901), MEXT Q-LEAP (JPMXS0118067426) for their financial supports.

Authors contributions

H.C., M.Lo., S.I., E.J. coordinated the project. T.A., H. I., Y. K. and S. I. performed and analysed the time-resolved reflectivity experiments. Y.N., H.K. measured the steady state reflectivity on thin films. V.TP. and R.S. built the setup for high pressure reflectivity, and with help of B.C. and D.B. measured the single crystal. A.J., V.-T.P, D.K., J.C.E., B.A. and J.L. developed the FemtoMAX setup for time-resolved X-Ray diffraction. R.M., J.G.-B., A.V., E.T., M.S., E.P., M.

A., E.J. and M. Lo. proposed the experiment at FemtoMAX and performed it with the help of local contacts. C.M., M.Le. and M.K. designed the ESRF tr-XRD experiment. J.G.-B., R.M., E.T., M.S., B.C., and E.J. performed the experiment at ESRF. R.M., J.G.-B., A.V. analysed tr-XRD data. D.B., J.T., B.C., E.J. and L.C. prepared and characterized the thin films and single crystals. H.C., M.Lo., S.I., E.J., B.C. and L.C. analysed and discussed closely about the whole results. H.C., M.Lo., S.I., E.J., wrote the manuscript with significant contributions from C.M. and E.P., critical reading from J.L., A.J., V.-T.P., and help from all coauthors.

Competing interest

The authors declare no competing interests.

Extended Data

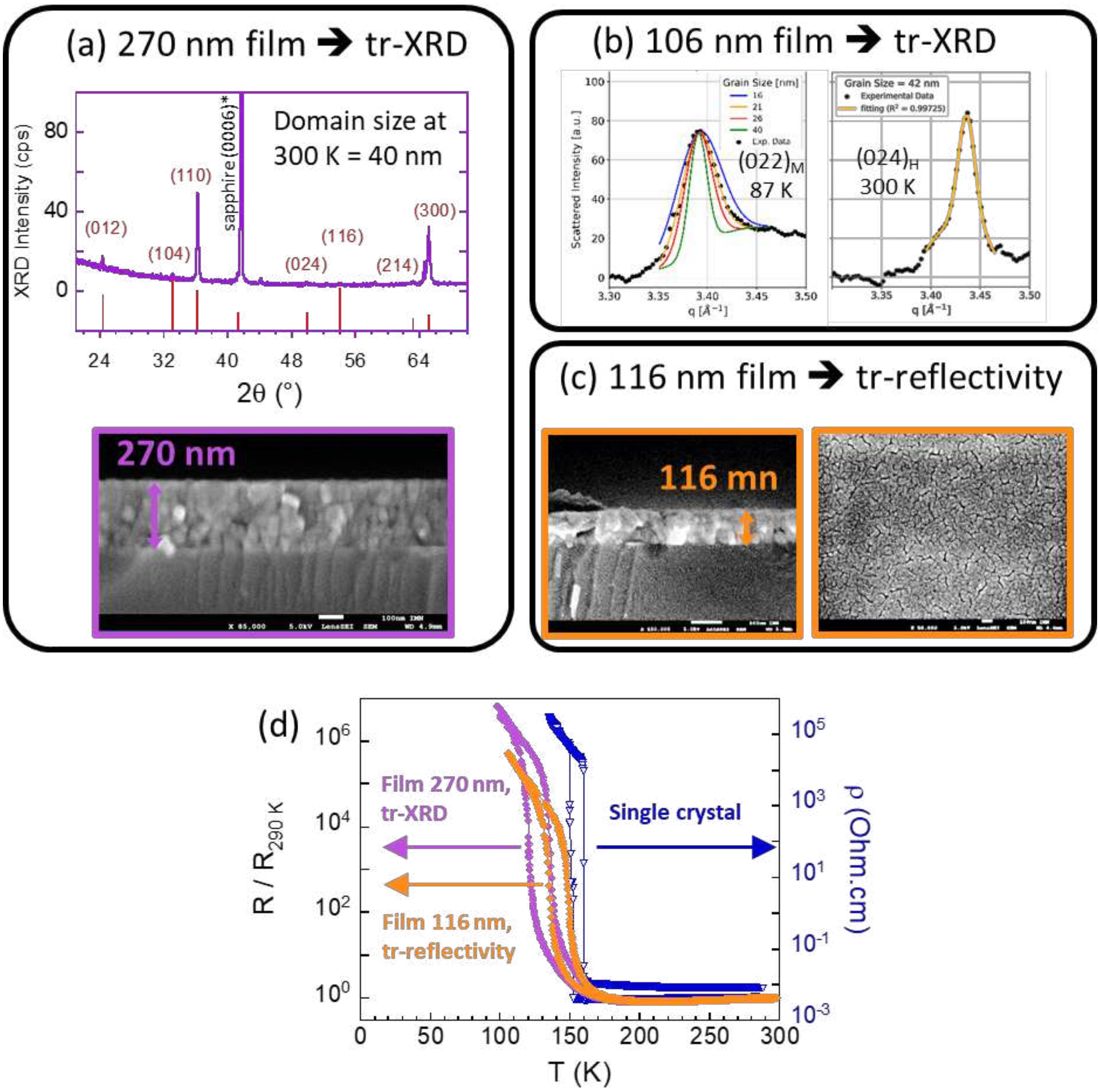

Extended data Fig.1 | Characterization of the V_2O_3 single crystal and thin films used in the work.

(a) top: steady-state X-Ray diffraction (XRD) pattern measured in a Bragg-Brentano geometry on the 270 nm thick film used for time-resolved XRD. The average crystallite size at room temperature, estimated by the Scherrer formula, is 40 ± 5 nm. Compared to theoretical intensities (red bars), the enhancement of (*hk0*) Bragg peaks with respect to (*hkl*) indicates a preferential orientation with the *c*-axis of the grains mostly oriented parallel to the substrate surface. Bottom: Scanning Electron Microscopy (SEM) image of a similar film prepared together with the previous one, but deposited on a SiO_2/Si substrate, and allowing a reliable estimate of the thickness. (b) XRD pattern of the 106 nm thick film used for tr-XRD both at ID09 and FemtoMAX beamlines. Zoom on the $(024)_H$ Bragg peak in PM phase, $(022)_M$ peak below the PM to AFI transition temperature, measured under steady state at ID09. A clear broadening of this Bragg peak appears in the monoclinic phase. Simulation of the $(022)_M$ Bragg peak leads to an estimate of the ferroelastic monoclinic domains size of 20±5 nm (➔ average radius = 10 ± 2.5 nm). This diffracting domain is half that at 300 K (see simulation of Bragg peak with a domain size of 40 nm). (c) SEM images (side and top views) of a 116 nm film prepared together with the one used for tr-reflectivity, but deposited on a SiO_2/Si substrate. (d) Temperature dependence of resistivity (single crystal) and resistance (thin films) of the samples used in this study. The large amplitude of the resistivity jump at the transition and the high transition temperature (160K upon heating) attest the quality and stoichiometry of the single crystal. Crystals from the same batch are used both for steady state and time-resolved reflectivity. The films show a jump of similar amplitude at the transition, with a slightly reduced transition temperature (147 K upon heating on the 116 nm thick film) as usually observed in V_2O_3 films. The absence of hysteresis below 120 K (tr-reflectivity thin film) and 107 K (tr-XRD) ensures the absence of phase coexistence in the different time-resolved studies performed in this work.

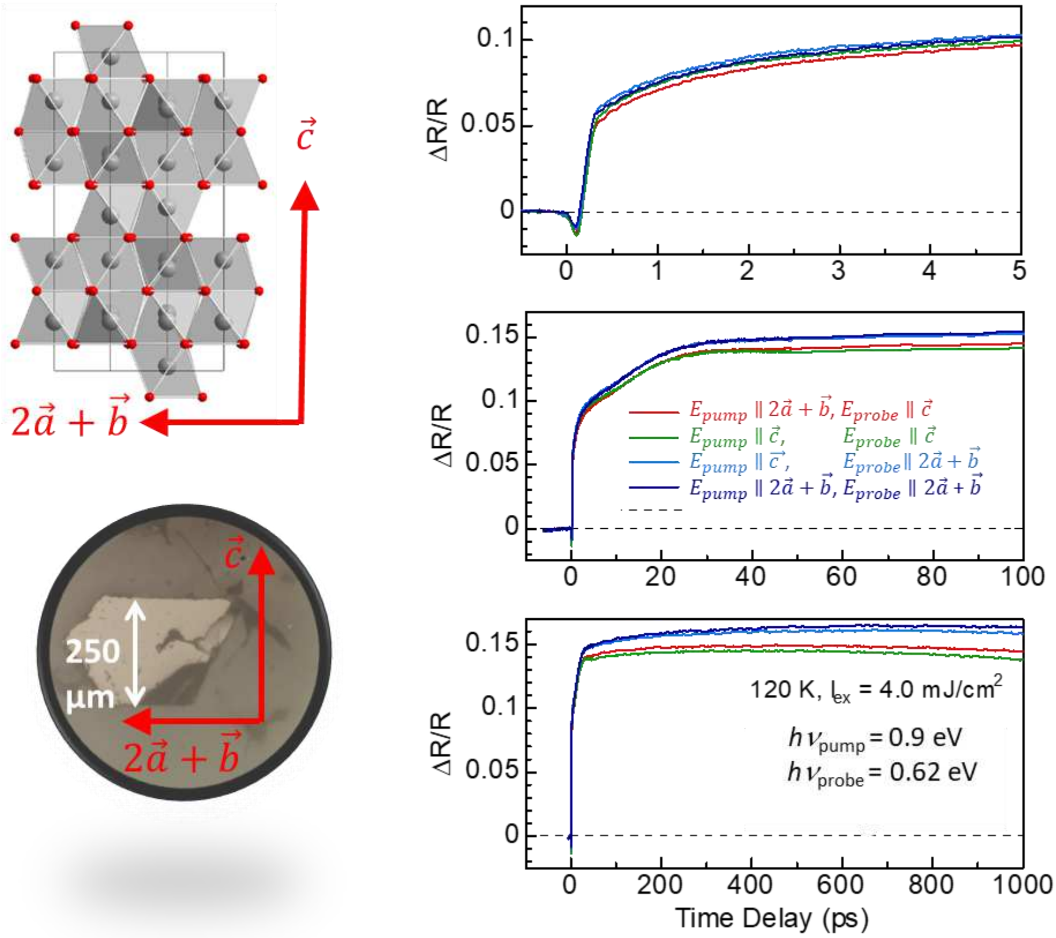

(a) (b)

Extended data Fig.2 | Effect of single crystal orientation and pump/probe laser polarization on time-resolved reflectivity in the AFI state of V_2O_3. In Fig.2 of the main article, we unveil a weaker photoinduced response of the single crystal with respect to thin film. In order to check if it results from an anisotropic response of V_2O_3, we have performed polarization dependent tr-reflectivity after a proper orientation of a V_2O_3 single crystal by XRD and a polishing to reveal a surface suitable for tr-reflectivitty. (a) optical image of the V_2O_3 crystal used for tr-reflectivity, with a surface defined by the the directions $\vec{c}$ and $2\vec{a}+\vec{b}$. (b) time-resolved reflectivity performed with polarization directions of the pump and the probe aligned along the $\vec{c}$ and $2\vec{a}+\vec{b}$ directions after photoexcitation at 4 mJ.cm^{-2} at 120 K. Overall, the polarization effect is very weak and is hence not the cause of the weaker photoinduced response of the crystal shown in Fig.2 of the main text.

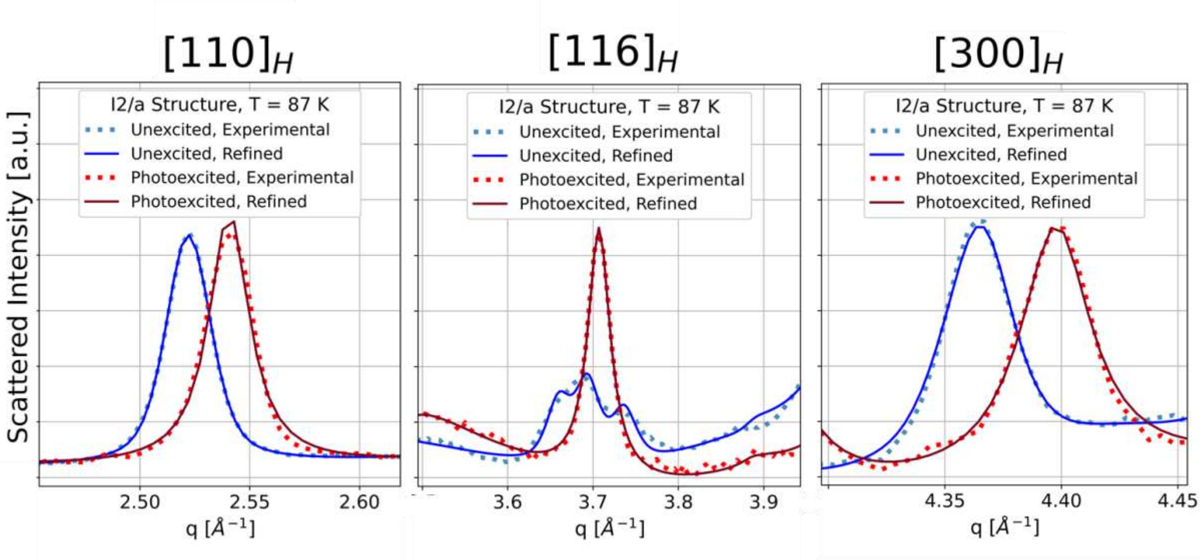

Extended data Fig.3 | X-Ray diffraction patterns measured at ID09 on V_2O_3 thin film (106 nm) at 87 K in the AFI monoclinic phase. The dashed lines correspond to XRD patterns without (blue) and with (red) photoexcitation of 10.5 mJ/cm^2 (delay 400 ps) converting 100 % of the volume into a metallic hexagonal phase. These XRD patterns were refined with Rietveld method (blue and red lines), allowing to extract the monoclinic cell parameters (space group 15, I2/a). We found for the unexcited initial phase:

a_M = 7.321(3) Å, b_M = 4.988(1) Å, c_M = 5.5325(28) Å, β = 96.96(2)°, V_M = 200.54(15) Å^3

and

a_M = 7.364(7) Å, b_M = 4.953(2) Å, c_M = 5.464(7) Å, β = 97.63(4)°, V_M = 197.54(15) Å^3 for the photo-excited phase 100 % converted into the hexagonal phase (delay = 400ps, fluence = 10.5 mJ/cm^2).

As the photo-conversion towards the hexagonal phase is complete, the photo-induced XRD pattern can equally be refined with a hexagonal unit cell, yielding a_H = 4.9505(6) Å, c_H = 13.966(6) Å and hence 2/3* V_H = 197.6 (2) Å^3.

Overall, the photoinduced volume change $\Delta V/V$ determined with this refinement procedure amounts to -1.50 ± 0.12 %.

However this refinement procedure is tedious and requires advanced corrections of sample to detector distance drifts. Therefore we used another strategy to estimate the volume change at any time delay and fluence, based on the simple Q shift of the (110)$_H$ Bragg peak. This is justified since:

(1) the photoinduced change of the pseudo-hexagonal c_H parameter (determined as $c_H = 2\sqrt{c_M^2 + \frac{1}{4}a_M^2 - a_M c_M \cos\beta}$) is as low as $\Delta c_H / c_H$ = -0.16 %, demonstrating that most of the volume change result from the large decrease of the pseudo-hexagonal a_H parameter,

(2) the refinement demonstrates that the two monoclinic Bragg peaks deriving from the $(110)_H$, *i.e.* the $(020)_M$ and $(211)_M$, are almost superimposed in the monoclinic phase $(Q_{(211)_M} - Q_{(020)_M} < 0.004\,\text{Å}^{-1})$.

As a consequence, the photoinduced shift ΔQ of the $(110)_H$ Bragg peak directly gives the relative change of the pseudo-hexagonal a_H parameter $\Delta Q/Q = -\Delta a_H/a_H$ and the relative volume change $\Delta V_H/V_H = 2\,\Delta a_H/a_H + \Delta c_H/c_H \approx 2\,\Delta a_H/a_H$. In the example shown in Extended Data Fig. 3, this method yields $\Delta V_H/V_H = -1.48 \pm 0.10\,\%$, in perfect agreement with the refinement method. All the estimate of the volume changes presented in Fig.3 and Fig.4 are obtained using this strategy.

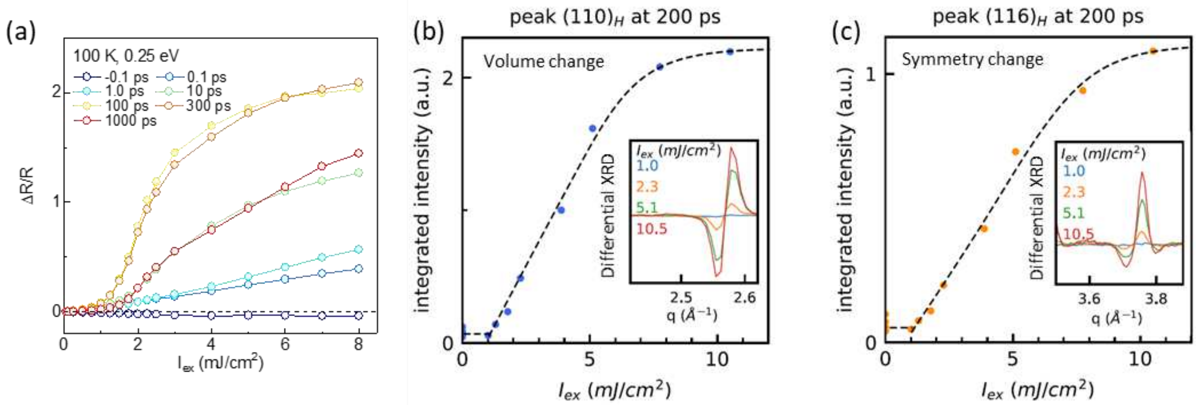

Extended data Fig.4 | Evolution of transient reflectivity and time-resolved XRD with fluence in the 85-100 K temperature range. (a) Evolution of transient reflectivity with fluence measured on the same 116 nm film as in Fig.3a, the same conditions (pump 0.89 eV, probe at 0.25 eV), but at 100 K instead of 10 K. (b) Fluence dependency of the volume change measured at 87 K on the 106 nm film (see Methods), as deduced from the integration of the differential XRD pattern around the $(110)_H$ Bragg peak for a pump-probe delay of 200 ps (c) Same as (b) for the symmetry change, deduced from the integration of differential XRD around the $(116)_H$ peak.

These three plots unveil a clear threshold fluence around 1 mJ/cm² above which the electronic part (a) and the structural components (b and c) of the insulator-to-metal transition are initiated. The threshold is reduced from 2.5 mJ/cm² at 10K (see Fig.3) to 1 mJ/cm² around 85-100 K

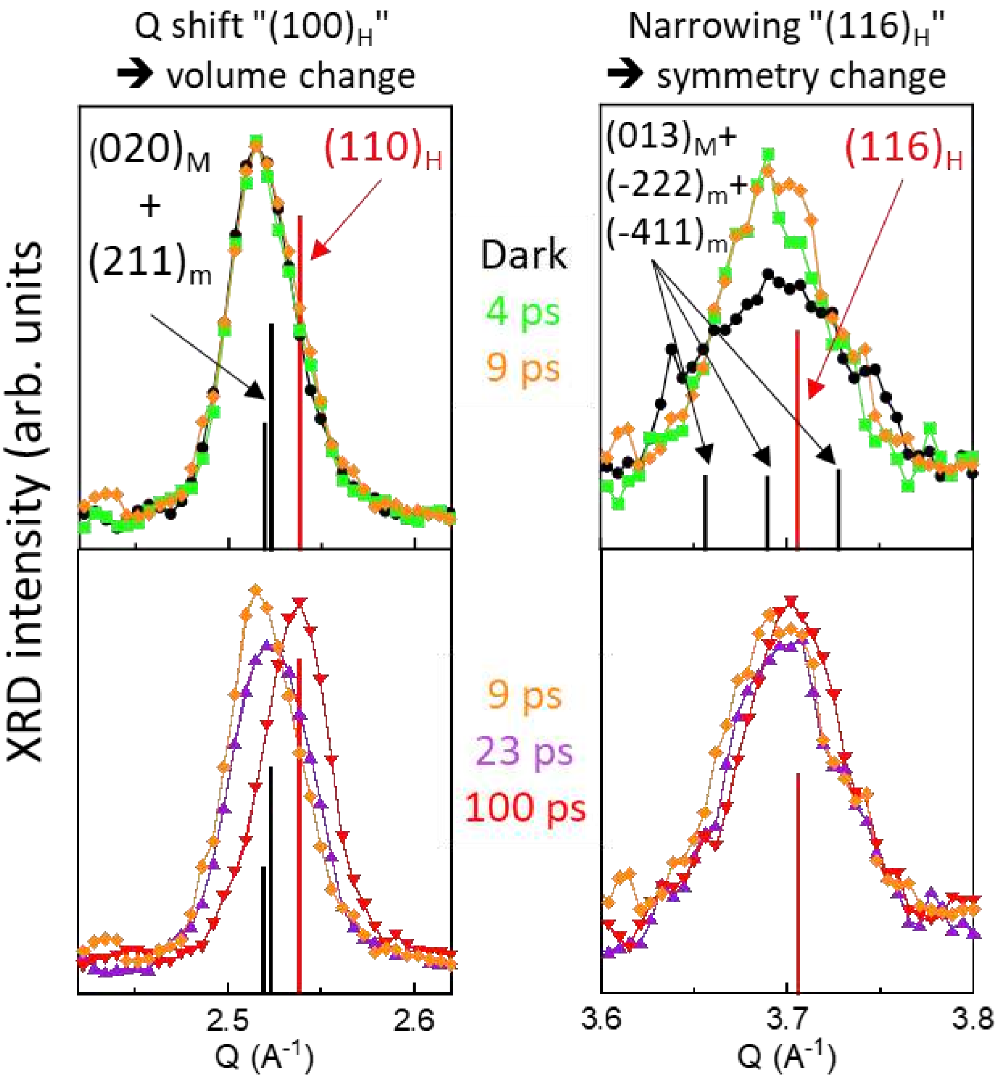

Extended data Fig.5 | **Evidence of different time scale for symmetry and volume change from time-resolvd XRD, measured at 10K on the 270 nm film at FemtoMAX.** (Left) Evolution of the $(110)_H$ Bragg peak for pump-probe delays shorter (top) and longer (bottom) than 9 ps. (Right) Same as right part for the $(116)_H$ Bragg peak, split into three peaks in the initial monoclinc state.

Vertical bars indicate the Bragg peak positions from the refinement of XRD pattern of the 116 nm film shown in Extended Data Fig.3, in black monoclinic, in red hexagonal phase. These panels evidence that the monoclinic to hexagonal transition is completed in less than 4 ps (see top right part), whereas volume change occurs slower after a onset shift of roughly 9 ps (left part).

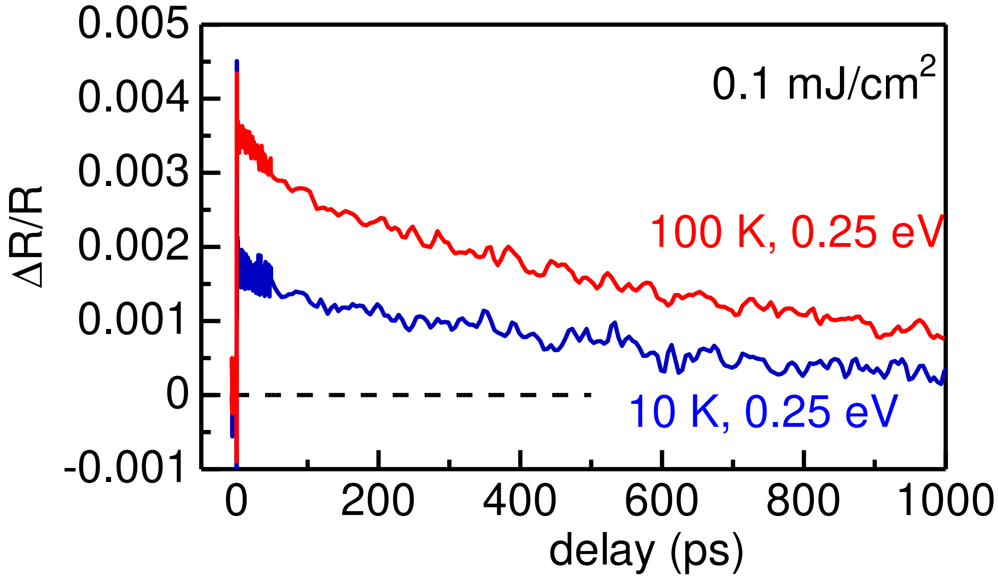

Extended data Fig.6 | Evidence of long-lived hot electronic states from transient reflectivity data. Time-resolved reflectivity measured at low pump laser fluence (0.1 mJ/cm^2, photon energy = 0.89 eV), showing electronic recombination time in the nanosecond range.
